Comprehensive Data Reduction for N₂O/HDPE Hybrid Rocket Motor Performance Evaluation

Landon Kamps [1,*,†]**, Kazuhito Sakurai** [1,†]**, Yuji Saito** [2] **and Harunori Nagata** [3]

[1]   Department of Mechanical and Space Engineering, Hokkaido University, Sapporo 060-8628, Japan;
      sakurai371@gmail.com
[2]   Department of Aerospace Engineering, Tohoku University, Sendai 980-8579, Japan;
      saito@aero.mech.tohoku.ac.jp
[3]   Faculty of Engineering, Hokkaido University, Sapporo 060-8628, Japan; nagata@eng.hokudai.ac.jp
[*]   Correspondence: landon_kamps@eis.hokudai.ac.jp; Tel.: +81-11-706-7226
[†]   These authors contributed equally to this work.

Abstract: Static firing tests of a hybrid rocket motor using liquid nitrous oxide (N₂O) as the oxidizer and high-density polyethylene (HPDE) as the fuel are analyzed using a novel approach to data reduction that allows histories for fuel mass consumption, nozzle throat erosion, characteristic exhaust velocity (c^*) efficiency, and nozzle throat wall temperature to be determined experimentally. This is done by firing a motor under the same conditions six times, varying only the burn time. Results show that fuel mass consumption was nearly perfectly repeatable, whereas the magnitude and timing of nozzle throat erosion was not. Correlations of the fuel regression rate result in oxidizer port mass flux exponents of 0.62 and 0.76. There is a transient time in the c^* efficiency histories of around 2.5 s, after which c^* efficiency remains relatively constant, even in the case of excessive nozzle throat erosion. Although nozzle erosion was not repeatable, the erosion onset factors were similar between tests, and greater than values in previous research in which oxygen was used as the oxidizer. Lastly, nozzle erosion rates exceed 0.15 mm/s for chamber pressures of 4 to 5 MPa.

Keywords: ballistic reconstruction technique; fuel regression; nozzle erosion; c^* efficiency

1. Introduction

Hybrid rockets are currently the focus of countless aerospace propulsion projects worldwide. Possibly the most prominent example is Virgin Galactic Ltd.'s hybrid rocket-powered spaceplane, "SpaceShipTwo", which is projected to begin commercial operations this year (FY2019) [1]. The attention on hybrid rocket development is justified by the logistical cost savings and risk reduction during operations of hybrid rockets compared to their liquid bi-propellant and solid rocket counterparts [2,3]. One potential use for the current state-of-the-art hybrid rockets is as apogee kick motors, which will alleviate satellite operators from relying solely on piggy-backing on larger satellite buses to destinations beyond geostationary transfer orbit (GTO), thus reducing launch wait times, and increasing freedom of movement to desired orbital placements.

Kuo and Chiaverini summarize the advantages of hybrid rockets for upper-stage use as having high specific impulse, throttling capability, safe manufacturing, and low cost [4] (p. 632). These attributes are especially attractive when considering the application of hybrid rockets as apogee kick motors. Jens et al. reported extensively on the concept of a hybrid rocket-powered apogee kick motor for placing CubeSats into deep space [5–7]. A key aspect of their proposed design is the storage of gaseous oxygen at very high pressures—roughly 50 MPa—to keep the storage volume at a minimum. Thus, one major technical limitation to such a vehicle is the maximum size and cost of the pressure

vessels necessary to store the oxidizer. In the case where payloads larger than CubeSats are desired, it may be advantageous to have a vehicle that uses an oxidizer that can be stored as a liquid to avoid the requirement for large and expensive pressure vessels.

Heister and Wernimont elaborate on the practicality of hybrid rockets for space applications which demand storable oxidizers, highlighting nitrous oxide (N_2O) for its low toxicity and self-pressurization ability [8]. To clarify the self-pressurizing ability of N_2O, values for density, ρ, in kg/m^3 and vapor pressure, P_v, in Pa are plotted as functions of temperature in Figure 1 based on data from the National Institute of Standards and Technology (NIST) online database [9]. The main conclusion that can be drawn from this figure is that N_2O can be self-pressurized as a liquid with densities ranging from 700 kg/m^3 to 900 kg/m^3 at pressures ranging from 4 MPa to 6 MPa for a range of temperatures typically permissible to satellite operators—roughly 280 K to 300 K.
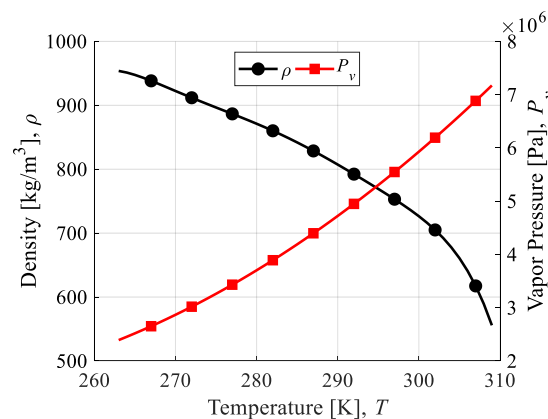

Figure 1. Thermodynamic properties of liquid nitrous oxide (N_2O).

Many noteworthy hybrid rocket demonstrations in recent years have been achieved in part by taking advantage of the self-pressurizing ability of N_2O. These include the aforementioned SpaceShipTwo, as well as its predecessor vehicle, SpaceShipOne [10], the highly successful Stuttgart University student-based hybrid sounding rocket, HEROS 3, reported by Kobald et al. [11], the rocket test sled trials of Muroran Institute of Technology reported by Nakata et al. [12], the small launch vehicles of TiSPACE Inc. reported by Chen and Wu [13], as well as the sounding rockets of Space Forest Ltd. reported by Gamal et al. [14]. However, it is also important to point out that N_2O can be pressurized above its vapor pressure to increase the flow rate capability of, and prevent two-phase flow within, the feed system. For example, Whitmore et al. used helium to pressurize a liquid N_2O feed system for closed-loop throttling and thrust control [15]. Similarly, the Peregrine sounding rocket project of NASA, Stanford University, and SPG Inc. reported by Zilliac et al. used helium to pressurize an N_2O reservoir to slightly above the vapor pressure [16]. The current research uses a similar feed system, which will be described in detail in the Materials and Methods section.

There are two distinct fuel design strategies used in the aforementioned N_2O hybrid rocket projects to achieve high thrust-to-weight ratios. One strategy is to use non-liquifying fuels with multiple ports and/or chambers to increase the burning surface area and/or create a vortex-like flow field. This is true for SpaceShipOne/Two, and the hybrid rockets reported by Chen and Wu, and Whitmore et al. in [1,13,15]. The other strategy is to use liquefying fuels with a single port, in which case the entrainment of liquid droplets from the surface of the melting fuel leads to high burning rates. This is true for the hybrid rockets reported by Kobald et al., Gamal et al., and Zilliac et al. in [11,14,16]. In a 5 kN thrust-class sounding rocket launch reported by Nagata et al., the former strategy was employed with great success using a high-density polyethylene (HDPE) fuel of the Cascaded Multistage Impinging-jet (CAMUI) design and liquid oxygen as the oxidizer [17]. With a characteristic exhaust velocity, c^*, efficiency, η^*, of 99% and a sustained acceleration during launch of 4 G to 5 G, the major concern of this development project shifted to nozzle thermochemical erosion. The tests in follow-on research

to investigate nozzle erosion consistently showed values of η^* greater than 95%. Furthermore, the mass "equivalent" regression rates, based on the fuel grain outer dimensions and mass consumption rates, reached values upwards of 3 mm/s, which is comparable to or exceeding that of liquefying propellants [18]. The main drawback of using a CAMUI-type fuel, or something similar in nature, is the rigor involved in the fuel design itself. It can be said that the main benefit of using liquefying fuels in place of geometrically complex fuels, like CAMUI, is the simplicity of the single port fuel design that can be used. Mazzetti et al. make a strong argument on behalf of hybrid rockets in general, but specifically for liquefying fuel-based hybrid rockets because of the combination of the high fuel regression rate and fuel design simplicity [19].

In the context of designing an apogee kick motor, achieving a high thrust-to-weight ratio becomes less critical than in the context of a planetary launch vehicle. For example, to achieve a transfer from GTO to Mars orbit, a change in velocity of roughly 1200 m/s is required. Even at a constant acceleration of only 1 G, this apogee kick would require only a two-minute burn time. Thus, it can be said that achieving a high specific impulse, low manufacturing costs, and minimal combustion oscillations is more important in the development of an apogee kick motor than improving the fuel regression rate. In fact, Jens et al. selected the non-liquefying fuel, polymethyl methacrylate (PMMA), over a liquefying wax fuel for their hybrid rocket apogee kick motor development specifically to prevent acceleration from exceeding 3 G [5].

In the fiscal year of 2018, the authors of this paper began the development of a hybrid rocket apogee kick motor in collaboration with the Japanese Institute of Space and Astronautical Science (JAXA/ISAS) that will be capable of transporting small satellites (less than 100 kg) from GTO to lunar orbits and beyond. Nitrous oxide (N_2O) was selected to be the oxidizer for its long-term storability, non-toxicity, non-corrosiveness, low cost, widespread commercial availability, self-pressurizing ability, and successful role in the numerous projects mentioned in the previous paragraphs. High-density polyethylene (HDPE) was also selected for its non-toxicity, low cost, and widespread commercial availability, as well as for its mechanical strength and heritage in the development of the CAMUI-type hybrid rocket by the authors and their predecessors.

The propellant combination, N_2O/HDPE, has mostly gone overlooked in previous research due to the heavy focus on the development of launch vehicles with high thrust-to-weight ratios. The latest version of the SpaceShipTwo engine may be an exception to this claim; however, the details of the current propellant combination have not been made public yet. The two previous publications that were closely related to the proposed work were an experimental study conducted by Doran et al. on a laboratory-scale N_2O/HDPE hybrid rocket [20], and a numerical study of nozzle thermochemical erosion conducted by Bianchi and Nasuti [21]. Doran et al. reported η^* values ranging from 90% to 95%, and a weak correlation between fuel regression rates—ranging from 0.4 mm/s to 0.6 mm/s—and oxidizer port mass flux. Bianchi and Nasuti predicted that the erosion rate of graphite is 0.06 mm/s when the equivalence ratio is close to 1 and the pressure is 1 MPa. Moreover, they demonstrated that as a general trend among all propellant combinations, the erosion rate decreases with an increasing equivalence ratio and is linearly dependent on pressure.

The results of Doran et al. and Bianchi and Nasuti serve as a valuable starting point for this research, but there are some reasons why this information is inadequate for our purposes. Doran et al.'s experiments had combustion times in the range of 5 s to 7 s, which is too short of a span to determine if the fuel regression correlations will remain true in time, yet long enough to introduce uncertainty due to the time-averaging of nonlinear terms needed for the correlations. For example, test 42 from Doran et al.'s study shows a duration of 5.9 s with an initial port diameter of 13.4 mm and an average regression rate of 0.76 mm/s. This means the oxidizer port mass flux decreased by roughly 40% during the test, which for this test would account for a span of almost 100 kg/m^2-s. Also, Doran et al. supplied N_2O to the motor as a gas, whereas it is crucial for the purposes of this study to supply the oxidizer as a liquid. Bianchi and Nasuti's results will prove to be consistent with this study, but they are only valid when the nozzle throat temperature has reached a steady state.

Due to the lack of previous work on the propellant combination of N_2O/HDPE, the authors found it necessary to conduct basic research to form empirical correlations for the fuel regression rate, c^*, efficiency, η^*, and nozzle erosion for the first time. Of the multitude of measurement techniques introduced in previous research, the latest versions of the data reduction methods referred to as ballistic reconstruction techniques appeared to offer the most effective means of pursuing this research in a cost-effective and expedient way. In general, ballistic reconstruction techniques only require some combination of the following commonly measured experimental values: (1) Oxidizer mass flow rate, $\dot{m}_{ox}$; (2) chamber pressure, P_c; (3) thrust, F; (4) overall fuel mass consumed, ΔM_{fu}; and (5) final nozzle throat diameter, $d_{t,f}$. This means that the same measurement equipment can be used regardless of fuel design, configuration, or scale. This is done by using either the c^* equation, thrust equation, or both, in an iterative algorithm to determine instantaneous values of the oxidizer-to-fuel mass ratio, ξ; c^* efficiency, η^*; thrust correction factor, λ; and, recently, nozzle throat area, A_t. Wernimont and Heister, and Nagata et al. introduced ballistic reconstruction techniques, which used the c^* equation to determine fuel mass consumption under the assumption that η^* is constant and nozzle throat erosion is negligible [22,23]. Carmicino and Sorge, and Nagata et al. alleviated the need to treat η^* as a constant by measuring thrust and incorporating the thrust equation [24,25]. Most recently, Kamps et al. combined these works, incorporating both the c^* and thrust equations, and treating η^* as a constant in order to determine the history of the nozzle throat area in an effort to investigate nozzle throat erosion [26]. This ballistic reconstruction technique was titled "Nozzle Throat Reconstruction Technique" or "NTRT," and was later used in a follow-on study by Kamps et al., which demonstrated how to use the results of the NTRT with thermocouple measurements from within the nozzle to determine the wall temperature history at the nozzle throat [27]. This follow-on technique was titled the "Throat Temperature Reconstruction Technique" or "TTRT."

Unfortunately, reconstruction techniques, such as the NTRT, have a region where multiple solutions exist for the results of ξ, typically when hybrid rocket tests are conducted in fuel-rich conditions. Nagata et al. [25] and Saito et al. [28] demonstrated that approximations for c^* can be used to overcome this problem in the data reduction of hybrid rocket firing tests using oxygen. However, as will be evident in the following section, these approximations are not suitable when using N_2O as the oxidizer because the region of multiple solutions that exists is too large. The objective of this research is to further develop the experimental methodology introduced by Kamps et al. so that the analysis of tests conducted under the propellant combination of N_2O/HDPE yields results for the histories of fuel consumption, nozzle erosion, and characteristic exhaust velocity efficiency regardless of the oxidizer-to-fuel-mass ratio. The purpose of this research is to lay the groundwork for effectively conducting basic combustion research in the development of a hybrid rocket apogee kick motor using N_2O as the oxidizer and non-liquefying fuels, such as HDPE, as the fuel.

2. Materials and Methods

Kamps et al. recently introduced a method, titled the "Nozzle Throat Reconstruction Technique (NTRT)," for determining both A_t and ξ histories through the data reduction of commonly measured experimental values with the aim of enabling hybrid rocket researchers to accurately and cost-effectively investigate nozzle erosion experimentally [26]. The two governing equations of this method are the thrust equation shown by (1), and the characteristic exhaust velocity equation shown by (2):

$$F = \lambda \dot{m} u_e + (P_e - P_a) A_e \tag{1}$$

$$c^*_{th} = P_c A_t / \eta^* \dot{m} \tag{2}$$

Here, the thrust, F, is in N and the theoretical characteristic exhaust velocity, c^*_{th}, is in m/s. The term, λ, is the dimensionless thrust correction factor, $\dot{m}$ is the propellant mass flow rate in kg/s, u_e is the nozzle exit velocity in m/s, P_e and P_a are the nozzle exit pressure and atmospheric pressure in Pa, and A_t and A_e are the nozzle throat area and exit area in m^2. The thrust correction factor, λ, accounts for

the momentum losses due to non-one-dimensionality and non-isentropicity of flow, as well as the momentum losses in the axial direction due to the divergence angle of the nozzle exit. The propellant mass flow rate can be shown in terms of the oxidizer-to-fuel-mass ratio according to Equation (3):

$$\dot{m} = \dot{m}_{ox}(1 + 1/\xi) \tag{3}$$

where the subscript, "*ox*", indicates that the mass flow rate term is a property of the "oxidizer" only.

When the propellant combination of N2O/HDPE is used, there exists a region of multiple solutions of ξ where maximum specific impulse can be achieved.

This is shown by breaking down the calculation of the thrust equation. The value of P_e is calculated implicitly from Equation (4):

$$\left(\frac{P_e}{P_c}\right)^{\frac{1}{\gamma}}\left(\frac{\gamma+1}{2}\right)^{\frac{1}{\gamma-1}}\sqrt{\frac{\gamma+1}{\gamma-1}\left(1-\left(\frac{P_e}{P_c}\right)^{\frac{\gamma-1}{\gamma}}\right)} = \frac{A_t}{A_e} \tag{4}$$

and u_e is calculated explicitly from Equation (5):

$$u_e = \eta^* c_{th}^* \sqrt{\frac{2\gamma^2}{\gamma-1}\left(\frac{2}{\gamma+1}\right)^{\frac{(\gamma+1)}{(\gamma-1)}}\left[1-\left(\frac{P_e}{P_c}\right)^{\frac{(\gamma-1)}{\gamma}}\right]} \tag{5}$$

where γ, the specific heat ratio of combustion gas, is calculated using the NASA Chemical Equilibrium with Applications (CEA) computer program as a function of P_c and ξ [29]. Although it is not a problem in the tests conducted in this study, it is worth noting that Equations (4) and (5) are not valid if shocks occur in the nozzle, which is possible in ground tests where the chamber pressure is relatively low. Figure 2 plots *F* as a function of ξ for the case where d_t is 4 mm, P_c is 4.7 MPa, and $\dot{m}_{ox}$ is 36 g/s—which is representative of the tests conducted in this study. Here, the efficiency terms, η^* and λ, were assumed to be 1 (i.e., 100%). The range of ξ from 4.0 to 7.1 results in roughly the same value for thrust. Specific impulse, I_{sp}, has also been plotted in Figure 2 to show that optimal performance is achieved when ξ is roughly equal to 7. This is important because in a typical hybrid rocket, the value of ξ increases in time. Thus, for the goal of maximizing I_{sp} in long duration firing tests, it may be advantageous to begin operations in the multiple solutions region of ξ. Furthermore, from the vantage point of nozzle erosion prevention, it is advantageous to operate with the smallest value of ξ that is possible [21].
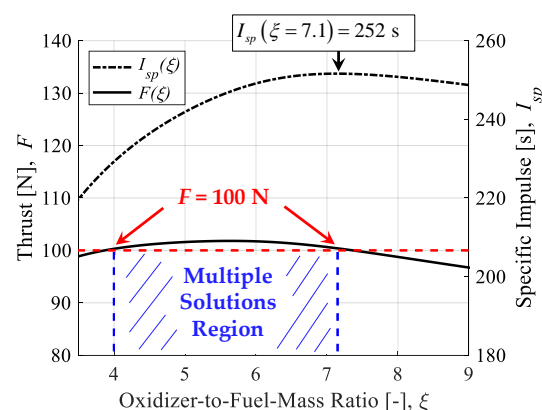

Figure 2. Example of multiple ξ solutions in the Nozzle Throat Reconstruction Technique (NTRT).

In previous data reduction methods, such as the NTRT, data are analyzed separately for each firing test conducted, with no cross-over of data between tests. However, in this research, a different approach is taken. The concept of the method employed in this paper is to include an additional experimental input in the governing set of equations of the NTRT, allowing for an additional output,

and avoiding the issue of multiple solutions arising from the thrust equation's dependency on ξ. More precisely, the value for overall fuel mass consumption, ΔM_{fu}, which is a constant value input to the original NTRT, will be replaced by a fuel mass consumption history, m_{fu}. Thus, η^* can be solved at every time, rather than be treated as a constant. Since the outputs of the data reduction method in this research are in effect the same as the NTRT, the method in this paper will be referred to as "NTRT plus" or "NTRT+."

The operational flow of the comprehensive data reduction procedure used in this research is shown in Figure 3. Data reduction steps are separated into "tiers" based on the information flow between operations. First, a firing test is repeated multiple times, varying only the combustion time between tests. In this way, a trendline can be determined that describes the overall fuel mass consumption progression between tests. This trendline is the only "tier I" operation. It is crucial that there is a clear agreement with the fuel mass consumption history trendline and the overall fuel mass consumption values determined through direct measurement in each test separately. With the fuel mass consumption history determined, it is possible to run all "tier II" operations: The NTRT+, NASA CEA, and fuel regression rate correlation operations. Finally, in this paper, the only "tier III" operation carried out is a simplification of the TTRT, which is used to determine the nozzle throat wall temperature histories.
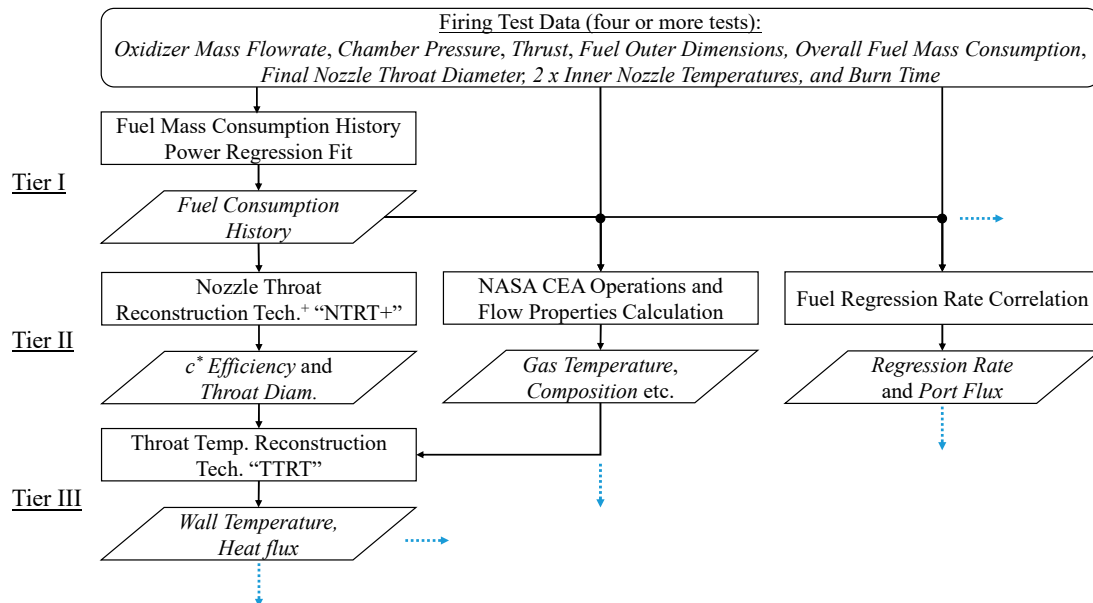

Figure 3. Flowchart of comprehensive data reduction operations in this research.

Although the set of governing equations for the NTRT+ is essentially the same as the original NTRT, the algorithm is significantly different. The computational flow of the NTRT+ is shown in Figure 4. There are two iterative loops: Loop A and loop B. Loop A iterations are conducted only once to solve for λ. Loop B iterations are conducted at every time step to solve for the η^* history. Convergence of loop A depends on reducing the final throat diameter residual, ψ_d, to zero, according to Equation (6):

$$\psi_d = \left| 1 - \frac{d_t(t_b)}{d_{t,f}} \right| = f(\lambda) \tag{6}$$

were $d_t(t_b)$ is the calculated value for the nozzle throat diameter at the end of the firing duration. The calculated nozzle throat diameter history is backed out of the value for the nozzle throat area, A_t, which is determined by rearranging the terms in Equation (2), as shown by Equation (7):

$$d_t = \sqrt{\frac{4}{\pi} A_t} = \sqrt{\frac{4}{\pi} \frac{\eta^* c_{th}^* \dot{m}}{P_c}} \tag{7}$$

The value of λ is iterated until the nozzle throat diameter calculation matches the known value at the end of the firing test. Convergence of loop B depends on reducing the thrust residual, ψ_F, to zero, according to Equation (8):

$$\psi_F(t) = \left| 1 - \frac{\lambda \dot{m}(t) u_e(t) + (P_e(t) - P_a) A_e}{F(t)} \right| = f(\eta^*(t)) \tag{8}$$

The value of η^* is iterated until the thrust calculation matches the measured value at that time.
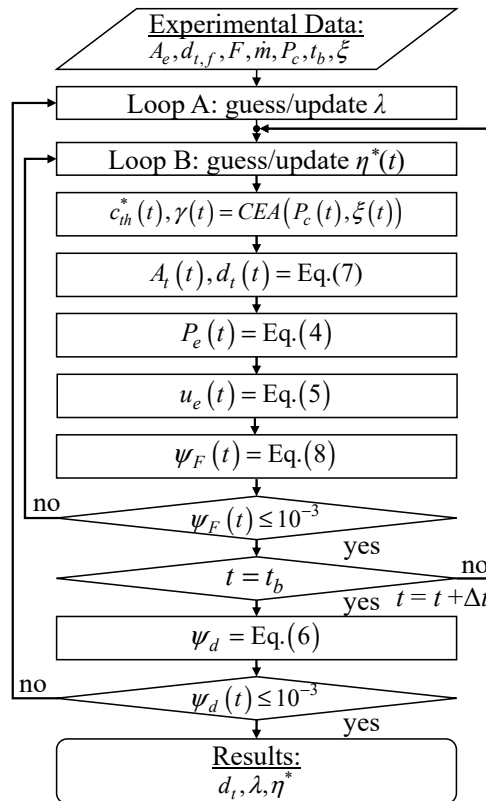

Figure 4. The NTRT+ algorithm computational flowchart.

The most common adaptation of Marxman et al.'s diffusion-limited regression rate model, first introduced in [30], will be used for the analysis in this study. This model is shown by Equation (9):

$$\dot{r}_{fu} = a G_{ox}^n = a \left(\frac{\dot{m}_{ox}}{\pi r_{fu}^2} \right)^n \tag{9}$$

where $\dot{r}_{fu}$ is in m/s, a and n are empirical constants, G_{ox} is in kg/m-s^2, and r_{fu} is the fuel port radius in m. Two methods of fuel regression rate correlations are compared in this study. In both cases, the concept behind the correlations is to run tests under the same oxidizer mass flow rate, varying only the combustion time. As the fuel burns, the port diameter will increase and the oxidizer port mass flux will decrease accordingly. This is different than the traditional approach of limiting the combustion time and varying the oxidizer mass flow rate to vary the oxidizer port mass flux. With that in mind, the correlation procedure remains essentially the same. The more conventional correlation procedure is to use only the endpoint data (i.e., changes in value before and after firing) for fuel mass consumption and the measurement of the oxidizer mass flow rate. This method is referred to as the "endpoint"

method. By separating the variables of the port radius, r_{fu} and time, t, Equation (9) can be integrated as follows in Equation (10):

$$\frac{\pi^n \left(r_{fu,f}^{2n+1} - r_{fu,o}^{2n+1} \right)}{(2n+1)} = a \int_0^{t_b} m_{ox}^n dt \cong a \sum m_{ox}^n \Delta t \tag{10}$$

where Δt represents the sampling rate of the experimental measurement history in s, and t_b is the burn time in s. Burn time is defined as the duration of time from the moment the (gauge) chamber pressure reaches 10% of the maximum value to the time at the aft-bisector of the pressure drop at the end of burning. This designation is outlined in [31] (p. 459), and was used in [26,27]. The fuel port radius in Equation (9) is calculated based on the fuel mass, M_{fu}, fuel density, ρ_{fu}, and the outer diameter and length of the fuel, D_{fu} and $L_{fu\neg}$, according to Equation (11):

$$r_{fu} = \sqrt{\frac{D_{fu}^2}{4} - \frac{M_{fu}}{\pi L_{fu}\rho_{fu}}} \tag{11}$$

where r_{fu}, D_{fu}, and L_{fu} are in m, M_{fu} is in kg, and ρ_{fu} is in kg/m^3. The constant, a, is determined by using the least-squares method (for a given value of n) on Equation (10), and the exponent, n, is determined by finding the value that maximizes the correlation of determination (i.e., R^2) of the results of a. The second fuel regression correlation method attempted in this paper simply considers the solution to Equation (11) for all times, and performs the least-squares method directly on Equation (9). This is possible because we can integrate the fuel mass consumption history trendline from the tier I operations to determine the history of M_{fu}.

The Throat Temperature Reconstruction Technique, or TTRT, employed in this study is a simplification of the method introduced in [27]. A single iterative loop solves for the nozzle throat wall temperature history, T_w. Convergence of the TTRT depends on reducing the thermocouple temperature residual, ψ_T, to zero:

$$\psi_T(t) = \left| 1 - \frac{T_{n1,calculation}(t)}{T_{n1,measured}(t)} \right| = f(T_w(t)) \tag{12}$$

Here, T_{n1} is the temperature at the position of the thermocouple placed closest to the nozzle throat in K. In general, the governing differential equation for 1D conductive heat flux in cylindrical coordinates reduces to Equation (13) by assuming a negligibly small axial temperature gradient and no internal heat generation:

$$\frac{\partial T}{\partial t} = \frac{\alpha}{r} \frac{\partial}{\partial r} \left(r \frac{\partial T}{\partial r} \right) \tag{13}$$

Here, α is thermal diffusivity of the nozzle in m^2/s, T is the local instantaneous temperature in K, and r is the radial position from the centerline of the nozzle in m. Approximating the partial derivatives in Equation (13) by the first term of the Taylor series expansions near the points of interest, consolidating terms, and rearranging yields the following finite difference equation:

$$\begin{aligned}
a_i^j T_{i-1}^{j+1} + b_i^j T_i^{j+1} + c_i^j T_{i+1}^{j+1} + d_i^j T_i^j &= 0 \\
a_i^j &= 2\alpha^j r_i \Delta t - \alpha \Delta r \Delta t \\
b_i^i &= -(4\alpha^j r_i \Delta t + 2r_i \Delta r^2) \\
c_i^j &= \alpha^j \Delta r \Delta t + 2\alpha^j r_i \Delta t \\
d_i &= 2r_i \Delta r^2
\end{aligned} \tag{14}$$

where Δt is the time step, subscript i specifies the radial node index, and superscript j represents the time index. Note that the thermal properties of graphite, k and α, are treated as functions of temperature, as described in the following paragraph, but this behavior is approximated by using the

solution of the temperature profile from the previous time step. With one temperature boundary set as the nozzle throat wall temperature, T_w, and the other set as the nozzle thermocouple measurement temperature, T_{n2}, we can solve for the temperature distribution history within the nozzle according to Equation (15):

$$
\underbrace{\begin{bmatrix} T^{j+1}_{w+\Delta r} \\ T^{j+1}_{w+2\Delta r} \\ \vdots \\ T^{j+1}_{r_{n2}-2\Delta r} \\ T^{j+1}_{r_{n2}-\Delta r} \end{bmatrix}}_{T_w \text{ at } j+1} = \underbrace{\begin{bmatrix} b^j_{w+\Delta r} & c^j_{w+\Delta r} & 0 & 0 & 0 \\ a^j_{w+2\Delta r} & b^j_{w+2\Delta r} & c^j_{w+2\Delta r} & 0 & 0 \\ 0 & \ddots & \ddots & \ddots & 0 \\ 0 & 0 & a^j_{r_{n2}-2\Delta r} & b^j_{r_{n2}-2\Delta r} & c^j_{r_{n2}-2\Delta r} \\ 0 & 0 & 0 & a^j_{r_{n2}-\Delta r} & b^j_{r_{n2}-\Delta r} \end{bmatrix}^{-1}}_{\text{Stiffness Matrix}} \underbrace{\begin{bmatrix} a^j_{w+\Delta r}T^j_{w+\Delta r} \\ a^j_{w+2\Delta r}T^j_{w+2\Delta r} \\ \vdots \\ a^j_{r_{n2}-2\Delta r}T^j_{r_{n2}-2\Delta r} \\ a^j_{r_{n2}-\Delta r}T^j_{r_{n2}-\Delta r} \end{bmatrix}}_{T_w \text{ at } j} - \underbrace{\begin{bmatrix} a^j_{w+\Delta r}T^j_w \\ 0 \\ \vdots \\ 0 \\ c^j_{r_{n2}-\Delta r}T^j_{n2} \end{bmatrix}}_{\text{Boundary}} \qquad (15)
$$

A mesh size of $\Delta r = 10^{-5}$ m and a time step of $\Delta t = 0.5$ s was used for the calculations in this study.

Static firing tests were carried out on a 100 N-thrust class motor. Depictions of the test setup, motor assembly, and fuel and nozzle schematics are shown in Figure 5a–c, respectively. The test setup consisted of three fluid supply lines in parallel: A main oxidizer line with an Ar gas tank and an N_2O reservoir; a purge gas line with an N_2 gas tank; and an ignition assist oxidizer line with an O_2 gas tank. The flow in each line was controlled using a Swagelok pneumatic ball valve operated by an SMC solenoid valve. Solenoid valve operations were controlled in LABVIEW7. The N_2O in the reservoir, which was stored at outdoor atmospheric temperature ($\approx$290 K), was pressurized to 7.6 MPa using Ar gas to ensure that it remained in a liquid phase until injection into the combustion chamber. The oxidizer mass flow rate was determined by measuring the pressure drop across an orifice plate with an orifice diameter of 1 mm located between the N_2O reservoir and the motor. The equation used to calculate oxidizer mass flow rate is (16):

$$
\dot{m}_{ox} = C_{or}\left(\frac{\pi}{4}d_{or}^2\right)\sqrt{\rho_{ox}\left(P_{up} - P_{dw}\right)} \qquad (16)
$$

where the oxidizer mass flow rate is in kg/s, C_{or} is a dimensionless orifice flow coefficient determined experimentally to be 0.92, d_{or} is the orifice hole diameter in m (i.e., 0.001 m), ρ_{ox} is the oxidizer density in kg/m^3, and P_{up} and P_{dw} are the pressure upstream and downstream of the orifice in Pa, respectively. Note that the density of N_2O is a function of temperature, and was calculated based on the following equation determined from the NIST database [9]:

$$
\begin{aligned}
\rho_{N_2O}(T) = \ & -(6.533 * 10^{-7})T^6 + (3.920 * 10^{-5})T^5 - (6.267 * 10^{-4})T^4 \\
& -(2.521 * 10^{-3})T^3 + (4.280 * 10^{-2})T^2 - (5.114)T + (907.7)
\end{aligned} \qquad (17)
$$

where, in this case, T is the temperature of N_2O in °C.

All tests were conducted using polyethylene (formula: C_2H_4) with a density of 955 kg/m^3 as the fuel. Fuel grains were assembled from multiple short cylindrical fuel blocks, which allowed for a pseudo-one-dimensional evaluation of the fuel mass consumption. As is shown in Figure 5b,c, the initial fuel port diameter of the first four blocks (blocks ①–④) was 20 mm and that of the last four blocks (blocks ⑤–⑧) was 30 mm. The step-increase in port diameter between blocks ④ and ⑤ was used to force a disturbance in the boundary layer and improve mixing. After assembly, fuel grains were loaded into glass fiber-reinforced plastic (GFRP) insulating tubes and sealed in a steel motor case. An impinging-type injector with 4 × 0.8 mm holes at a convergence angle of 45° was used to promote atomization. The nozzles used in all tests were manufactured using the same grade of isotropic graphite, Tokyo Tokai Carbon Ltd. G347. The density and thermal conductivity at atmospheric conditions are listed by the manufacturer to be $\rho_n = 1850$ kg/m^3 and $k = 116$ W/m-K, respectively [32]. The temperature dependency of these and other properties of G347 graphite is not specified by the

manufacturer, and so values were referenced from previous research on similar graphite. An empirical correlation of data for thermal conductivity, k, based on Figure 1 in [33] yields Equation (18):

$$k(T) = (3712)T^{-0.602} \text{ for } 200 < T < 2500 \tag{18}$$

and an empirical correlation of data for specific heat, c_p, based on Figure 1 in [34] yields Equation (19):

$$c_p(T) = (651)\ln(T) - 2877 \text{ for } 200 < T < 3000 \tag{19}$$

where k is in W/m-K, c_p is in J/kg-K, and T is in K. The initial nozzle throat diameter, $d_{t,o}$, was 4 mm in all tests, and the nozzle exit diameter, d_e, was 8 mm in all, but one test. The nozzle exit diameter in a single test was lowered to 6 mm to examine the effect of the nozzle expansion ratio, ε, on the nozzle throat erosion history and thrust correction factor. Thus, in all tests, with the exception of one, ε is 4, and in one test, ε is 2.25. There are three thermocouple measurement ports at the nozzle throat plane. The initial radial distances from the thermocouple measurement points to the throat are 5 mm, 8 mm, and 10 mm, as shown in Figure 5c.
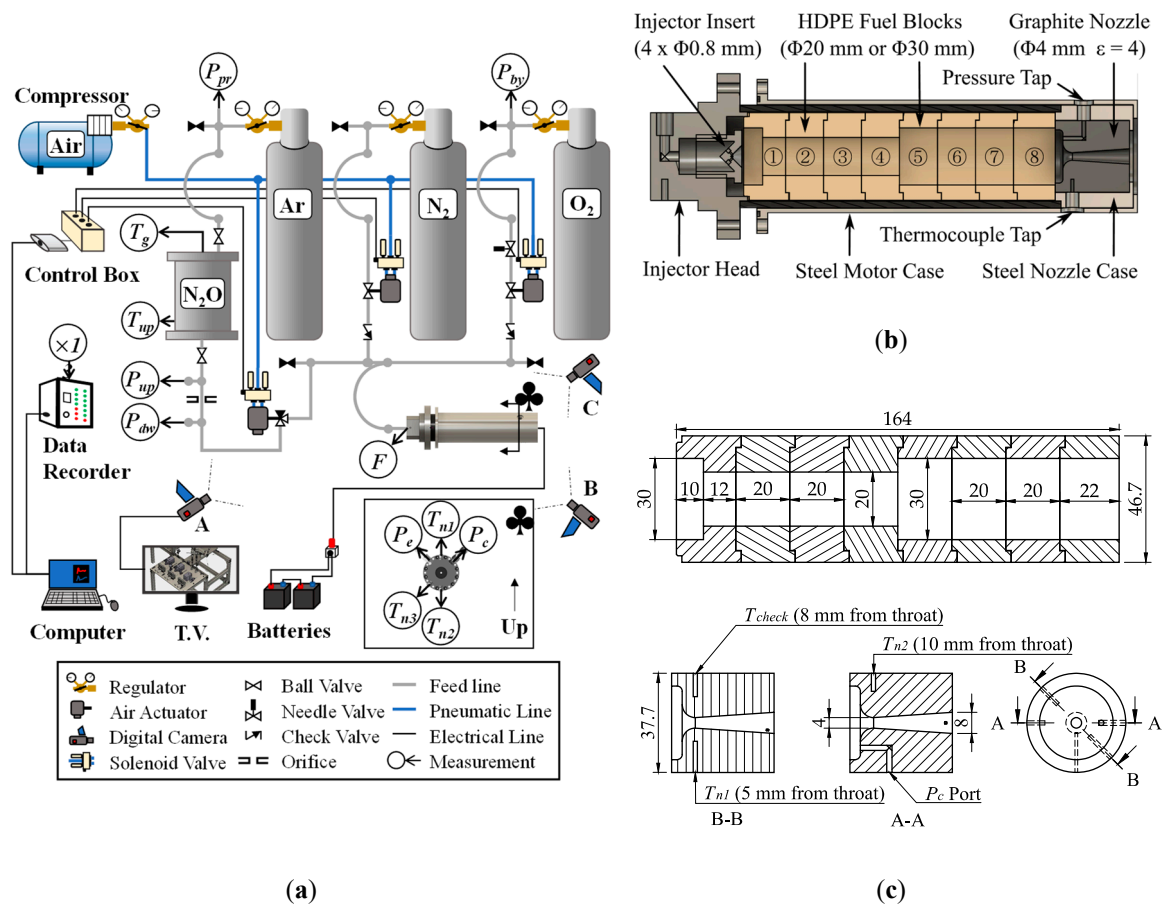

Figure 5. The experimental apparatus (**a**) test setup; (**b**) cut-away view of the motor assembly; (**c**) detailed schematics of the fuel grain and nozzle (units of mm).

The three digital cameras labeled "A", "B", and "C" in Figure 5 were used to monitor key components of the test apparatus at all times. These cameras were displayed on a T.V. located in a concrete bunker near the test stand. The T.V., computer, control box, and batteries were operated from a desk within the bunker. A depiction of the test sequence using screenshots from camera "B" (see Figure 5a) is shown in Figure 6. In all tests, ignition was achieved by sending an electrical current through a coil of nichrome wire affixed to the lip of the first fuel block using 1 g of an epoxy gunpowder

mixture: 0.8 g epoxy and 0.2 g gunpowder. Wire leads were fed through the nozzle exit and attached to a DC voltage source. A test section of wire and nichrome coil was attached in series to the main ignition line to allow for a visual confirmation that the current was large enough to heat the nichrome wire. Nichrome wire was heated for 10 s before actuating the oxidizer supply valve and initiating the firing test. Ignition was first achieved using 2 s of a flow of 1 g/s of gaseous oxygen (O_2) to ensure heating and gasification of fuel. After two seconds of O_2 ignition, the O_2 line was closed, and the main oxidizer (N_2O) line was opened. Firing tests were shut down by closing the N_2O line and opening the N_2 purge line. The chamber was purged with N_2 for a minimum of 30 s, both to extinguish the combustion of fuel and to cool the nozzle to less than 500 K for handling.
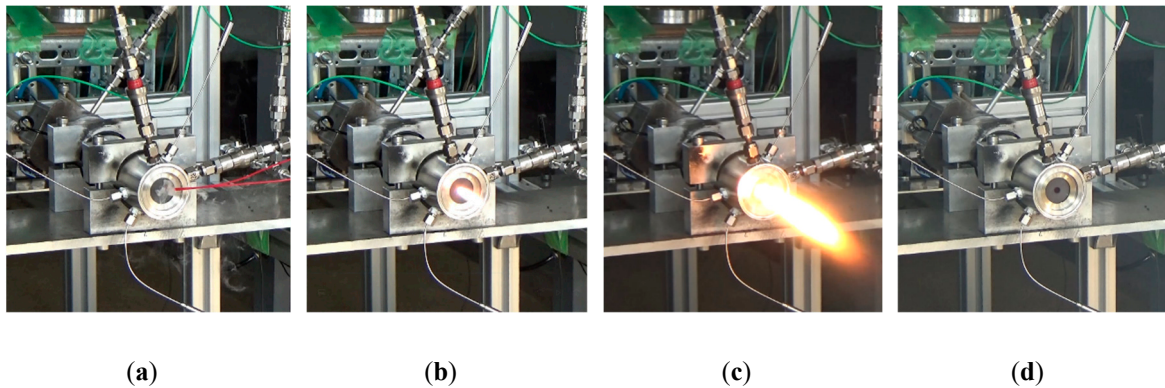

(a)　　　　　　　　**(b)**　　　　　　　　**(c)**　　　　　　　　**(d)**

Figure 6. Screenshots of the firing test sequence (**a**) nichrome wire heating (0 s to 10 s); (**b**) O_2 ignition assist (10 s to 12 s); (**c**) main burn (12 s to $12 + t_b$ s); (**d**) N_2 purge/cooling (12 s $+ t_b$ s $+ 30$ s).

As required for the NTRT+ and TTRT, multiple dynamic and static measurements were taken during the experiments conducted in this study. Pressures were measured using KYOWA DCS-10 MPa and KYOWA DCS-5 MPa pressure sensors with rated accuracies of ±40 kPa and ±28 kPa, respectively. Thrust was measured using a KYOWA LMB-A-200N load cell with a rated accuracy of ±3.5 N. These instruments were calibrated by the manufacturer such that the rated accuracies account for uncertainty due to nonlinearity, hysteresis, low-temperature conditions, and external loading. Nozzle temperatures were measured using RC Pro k-type thermocouples rated up to a temperature of 1100 °C, which exhibited a response time of 0.3 s. Dynamic measurements were recorded at 200 Hz using DCS-100A series software, and later filtered using a 20-point moving average. The reason for applying a moving average was to reduce the presence of oscillations in the reconstructed nozzle throat erosion histories. The uncertainty introduced by applying such moving averages is much smaller than the precision limits of the sensors used, and therefore will not be addressed in detail in this paper (refer to [26]). Initial and final nozzle throat diameter measurements, $d_{t,o}$ and $d_{t,f}$, were taken by the image analysis of digital photographs of the nozzle before and after firing. A length scale was established by placing a plaque of 1 mm-spacing grid paper next to the nozzle being photographed. The nozzle throat diameter was computed based on the area of the lighted region at the throat using ImageJ software [35].

Uncertainty in the experimental measurements of thrust, pressure etc. propagates through the tiers of the comprehensive data reduction operations. The details of this process can be summarized by Equation (20), which expresses the overall uncertainty, U_y, in some operational output, y, as a function of the inputs, x_i:

$$U_y = \sqrt{\sum \left(\frac{\partial y}{\partial x_i} U_{x_i} \right)^2} \tag{20}$$

Here, the U_{xi} terms on the right-hand side represent the uncertainties in the x_i measurements. The partial derivative terms in Equation (20) represent the sensitivity of the reconstructed solution to each

input. Since the algorithms in most of the data reduction operations are coupled non-linear problems, the partial derivative terms in Equation (20) are approximated as (21):

$$\frac{\partial y}{\partial x_i} \cong \frac{y(101\% x_i) - y(100\% x_i)}{1\% x_i} \tag{21}$$

Here, the numerator is the change in value of solution y given that the input parameter, x_i, has been perturbed by the amount of 1% of the nominal value.

3. Results

Six firing tests were conducted for this study in total. A summary of the experimental results is shown in Table 1. These tests have been labeled according to their burn times for plotting and comparison purposes. The local names of these tests are listed in the second column of Tables 1 and 2 for continuity. Test-3s, 4s, 10s-I and 15s were conducted with the aim of determining the fuel mass consumption trendline necessary for comprehensive data reduction operations. Test-10s-II and Test-10s-III were conducted to assess the repeatability of fuel mass consumption and nozzle throat erosion of Test-10s-I. In Table 1, the change in the nozzle throat diameters due to thermochemical erosion, Δd_t, are listed in mm, the values of overall fuel mass consumption, ΔM_{fu}, are listed in g, the time-averaged thrusts, $\overline{F}$, are listed in N, the time-averaged oxidizer mass flow rates, $\overline{\dot{m}}_{ox}$, are listed in g/s, the time-averaged chamber pressures, $\overline{P}_c$, are listed in MPa, and the time-averaged nozzle temperatures, $\overline{T}_{10mm}$, $\overline{T}_{8mm}$, and $\overline{T}_{5mm}$, are listed in K. An inspection of the overall fuel mass consumption and final nozzle throat diameters of Tests-10s-I through to III reveals that nozzle throat erosion was not the same even though the initial test conditions were identical, whereas the values of fuel mass consumption were within 1% of one another. Test-3s did not have a measurable amount of nozzle throat erosion, whereas the remaining tests did. The primary reason for this is that the nozzle throat wall temperature did not become high enough to allow for chemical reactions with the combustion gas. This is further discussed in Section 3.4. The greater than symbol ">" means that the thermocouple overheated during the firing, and thus the time-averaged temperature shown is an underestimate of the true value.

Table 1. Summary of direct measurements and their uncertainties.

Test Label	Local Name	Δd_t mm	ΔM_{fu} g	$\overline{F}$ N	$\overline{\dot{m}}_{ox}$ g/s	$\overline{P}_c$ MPa	$\overline{T}_{10mm}$ K	$\overline{T}_{8mm}$ K	$\overline{T}_{5mm}$ K
3s	(CBX-5)	0.05 ± >100%	30 ± <1%	74 ± 4%	41 ± 4%	4.1 ± 1%	518	551	661
4s	(CBX-4)	0.20 ± 50%	35 ± <1%	78 ± 4%	41 ± 4%	4.1 ± 1%	520	570	717
10s-I	(CBX-6)	0.53 ± 20%	74 ± <1%	81 ± 4%	39 ± 4%	4.2 ± 1%	551	>582	>745
10s-II	(CBX-8)	0.75 ± 10%	73 ± <1%	89 ± 4%	38 ± 4%	4.4 ± 1%	710	776	>874
10s-III	(CBX-9)	1.00 ± 10%	74 ± <1%	83 ± 4%	39 ± 4%	4.1 ± 1%	556	600	>764
15s	(CBX-7)	0.80 ± 13%	110 ± <1%	88 ± 4%	37 ± 4%	4.3 ± 1%	658	>723	>859

Note: Time averages were taken for the entire burning duration, and the greater than symbol, >, is used in the case where thermocouples overheated during the test.

The unprocessed pressure cascade and thrust histories are plotted together in Figure 7a,b. The main steps in the test sequence (as shown in Figure 6) have also been labeled in Figure 7a. It is evident that all tests show the same pressure and thrust to within less than ±2.5% up to 15 s into the test sequence (i.e., the end of burn in Test-3s), but the pressure and thrust histories beyond 15 s were not the same. This means that the primary cause of the differing values of pressure and thrust in tests lasting longer than Test-3s were due to the differences in the nozzle throat erosion history. Figure 7b shows an expanded view of the first 4 s of ignition and start-up transients. Each test reached a steady state around 14 s into the test sequence after a transient lasting 2 s. There is a sharp increase that ends the transient between 13 s and 14 s into the firing sequence. The timing of this increase varies between tests, although the rate and trend of the increase is similar.
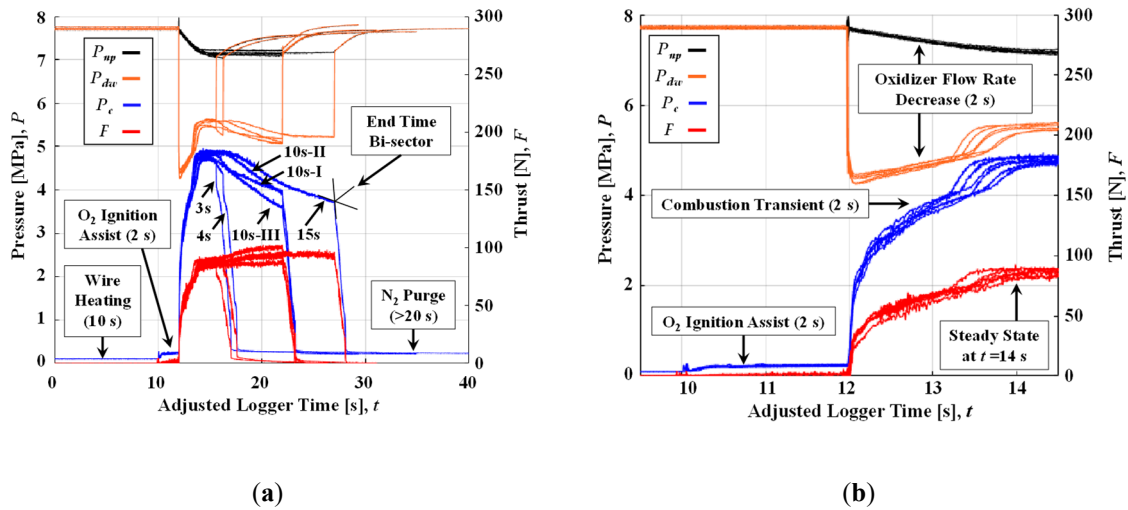
(a)　　　　　　　　　　　　**(b)**

Figure 7. Unprocessed static firing test data of all tests; (**a**) the first 40 s of the firing sequence, (**b**) expanded graph of the first 4 s of ignition and start-up transients.

3.1. Tier I Results: Fuel Mass Consumption History Trendline

The overall fuel mass consumption and the associated trendline is plotted for all tests in Figure 8a. A power-type trendline yields a near perfect fit for the fuel mass consumption history, in which the fuel consumption of Tests-10s-I to III were within ±1% of one another. This high degree of repeatability is important for the NTRT+, which operates on the assumption that the trendline in Figure 8a accurately represents the fuel consumption history of any given test. Figure 8b shows the overall fuel regression by block in all tests in units of meters. These values were calculated based on the change in mass, according to Equation (11). Blocks ①–④ had a greater overall fuel regression than blocks ⑤–⑧ in all tests. This can be explained by the fact that the first four blocks have a smaller initial port diameter, and thus a larger oxidizer port mass flux. However, it is also interesting to point out that block ① and block ⑤, both of which have step changes in port diameter, regressed less than similar blocks downstream.
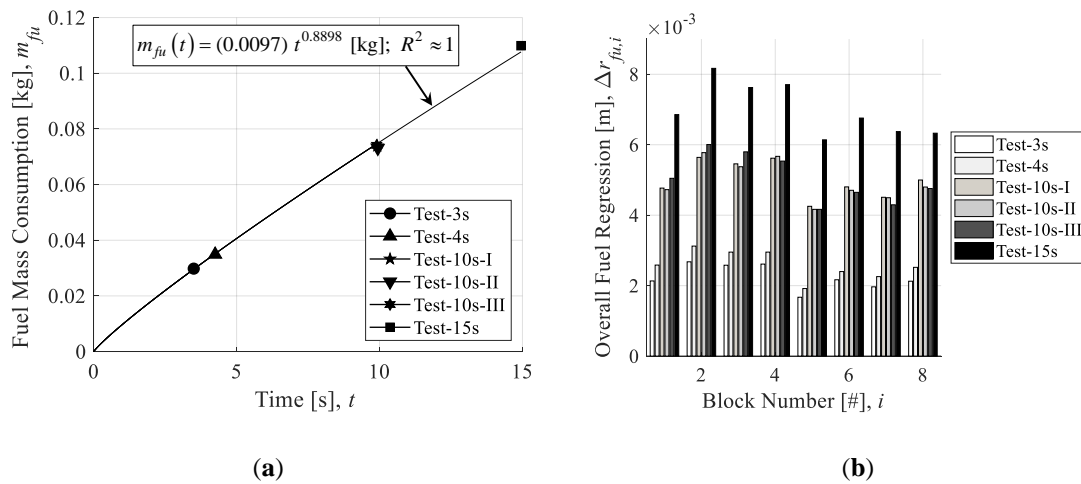

(a)　　　　　　　　　　　　**(b)**

Figure 8. Fuel consumption analysis (**a**) fuel mass consumption trendline; (**b**) fuel regression by block.

Block ① is immediately downstream of the injector, and thus marks the initiation point of the boundary layer. Reduced fuel regression rates at this location should be expected because the boundary layer is not fully developed. It is implied in the numerical analysis conducted by Kumar and Kumar [36], and by Kumar and Ramakrishna [37] that step increases in fuel port diameter are also likely to create recirculation zones downstream of the disturbance. The results in Figure 8b are consistent with this

analysis. The reduced fuel regression in block ⑤ can be explained by the presence of a recirculation zone, downstream of which fuel regression increases again. In following, the local peaks in the fuel regression of blocks ② and ⑥ are the result of increased turbulent heating downstream of the recirculation zones of blocks ① and ⑤, respectively.

3.2. Tier II Results

3.2.1. Fuel Regression Correlations

In the same way that the fuel mass consumption history trend line had a nearly perfect fit (with a coefficient of determination of ≈ 1), the "endpoint" fuel regression correlation led to a near perfect fit, as shown in Figure 9a. In the "history" method, where the histories of fuel regression rate are plotted directly against the histories of port mass flux, the resulting regression correlation has a coefficient of determination of 0.95, as shown in Figure 9b. This figure is organized according to the left- and right-hand side of Equation (9), so it is possible to plot and compare all correlations introduced so far in this figure. The waviness that appears in the first three seconds of the fuel regression rate histories is the result of the decrease in the oxidizer mass flow rate in the beginning of each firing due to the chamber pressure transient, as seen in Figure 7. DeLuca et al. [38], Pavaran et al. [39], and Evans et al. [40] examined time-resolved burning rates using direct (optical) measurements and did not observe this degree of waviness. The general trend that fuel regression rate decreases in time with decreasing oxidizer port mass flux is in agreement with [38–40].
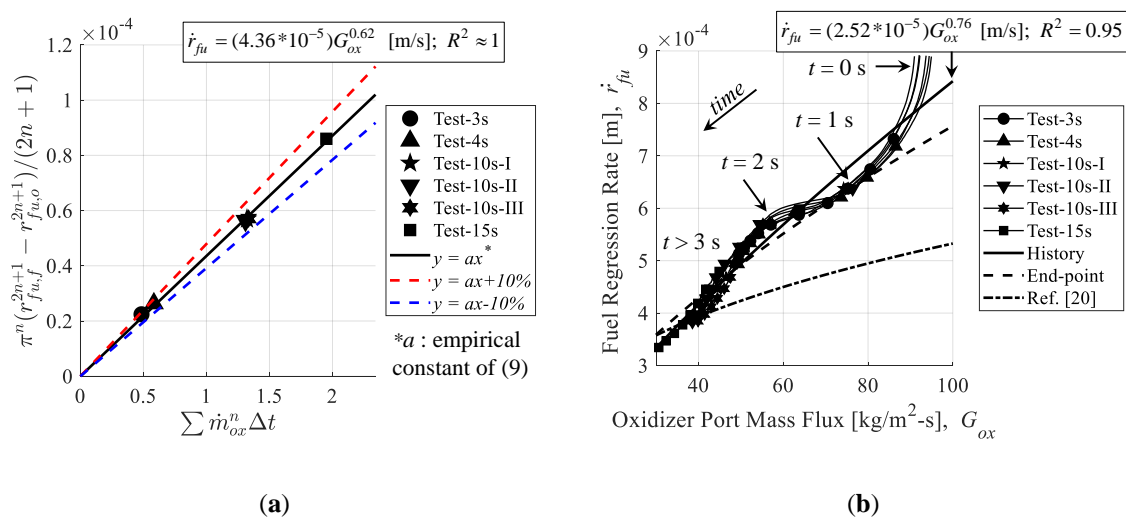

Figure 9. Fuel regression rate correlations of (**a**) endpoint correlation; (**b**) history correlation.

It can be seen from Figure 9b that the endpoint correlation slightly underestimates the values of the histories, and the results of Doran et al. grossly underestimate the magnitude and slope of these histories when $G_{ox} > 50$ kg/m^2-s. The most important discrepancy is the large difference in the solution of the fuel regression rate exponent, n. The history correlation results in an exponent of 0.76, which is very close to the theoretical value of 0.8 that is expected by Marxman et al.'s diffusion-limited boundary layer combustion theory [30,41], whereas the endpoint method results in an exponent of 0.62, and Doran et al. reports a value of 0.331 [20]. The departure of the fuel regression correlation exponent, n, from a value of 0.331 in Doran et al.'s study [20] to either 0.62 or 0.76 in this study, depending on whether the endpoint method or history method is used, warrants a discussion.

There does not appear to be a very large difference in the test apparatus used in each study. One reason for this discrepancy may simply be that the range of G_{ox} tested in this study is too narrow. The time-averaged values of G_{ox} varied from 50 kg/m^2-s to over 300 kg/m^2-s in Doran et al.'s test series, but only from 50 kg/m^2-s to 100 kg/m^2-s in this study. With that stated, it is also clear from this study that

the largest changes in G_{ox} take place in the first three seconds of firing, which constitute half of the burn time in Doran et al.'s tests. Given that even the time-averaged endpoint values from this study overestimate the prediction of Doran et al. by nearly 50%, it seems possible that the low exponent observed by Doran et al. may simply be due to the uncertainty introduced by using time-averaged values in the fuel regression rate correlation of Equation (9). If so, the consequences of this are grave, because the increase or decrease in time of the value of ξ depends on whether the exponent, n, is greater than or less than 0.5. In other words, the results of this study will predict an increase in ξ in time, whereas the results of Doran et al. will predict a decrease of ξ in time.

It is important to point out that although the fuel regression is being calculated based on the fuel mass consumption (refer to Equation (11)) and thus does not directly consider the shape and orientation of the burning surface at the end surfaces near the injector in block ① and at the end face of block ④, the combined surface area of these end faces is a mere 1% of the main port burning surface area. As the fuel burns and all surfaces blend together with the main port, any possible effects are reduced even further. Thus, the effect of these non-tubular burning surfaces is considered to be negligible for the sake of the analysis presented here.

3.2.2. Results of the NTRT+

The results of the NTRT+ for thrust correction factor, λ, and time-averaged c^* efficiency, $\overline{\eta}^*$, are listed in Table 2. The results of the NTRT+ for oxidizer-to-fuel-mass ratio, ξ, history are shown in Figure 10a, while the results for nozzle throat diameter history, d_t, and c^* efficiency history, η^*, are shown in Figure 10b. The histories of the oxidizer mass flow rate, $\dot{m}_{ox}$, were added to Figure 10a to show that increases in $\dot{m}_{ox}$ correspond to increases in ξ. The close agreement of all throat diameter histories with the known value for $d_{t,o}$ in the beginning of the tests bolsters the reliability of the NTRT+ results, since $d_{t,o}$ is a known value that is not used in the NTRT+ algorithm. It can be seen from these results that the timing of the onset of nozzle throat erosion varies by 2 s between tests, from around 3 s in Tests-4s and 10s-I to around 5 s in Tests-10s-II and 15s. Also, the erosion rate of Test-10s-I is noticeably smaller than that of the other tests. Test-10s-I is the one test which employed a smaller nozzle expansion ratio than the other tests—2.25 versus 4.0. Thus, it is likely that the nozzle expansion ratio effected some aspect of the nozzle throat erosion mechanisms. Similar to the chamber pressure and thrust histories, the histories of η^* were the same during the first three seconds of burn time, during which time they sharply rose to a steady-state value. The time averages of the steady-state values of η^* are listed in Table 2. The values differ between tests in the range of $0.85 < \eta^* < 0.95$, which is consistent with the results of Doran et al. [20].
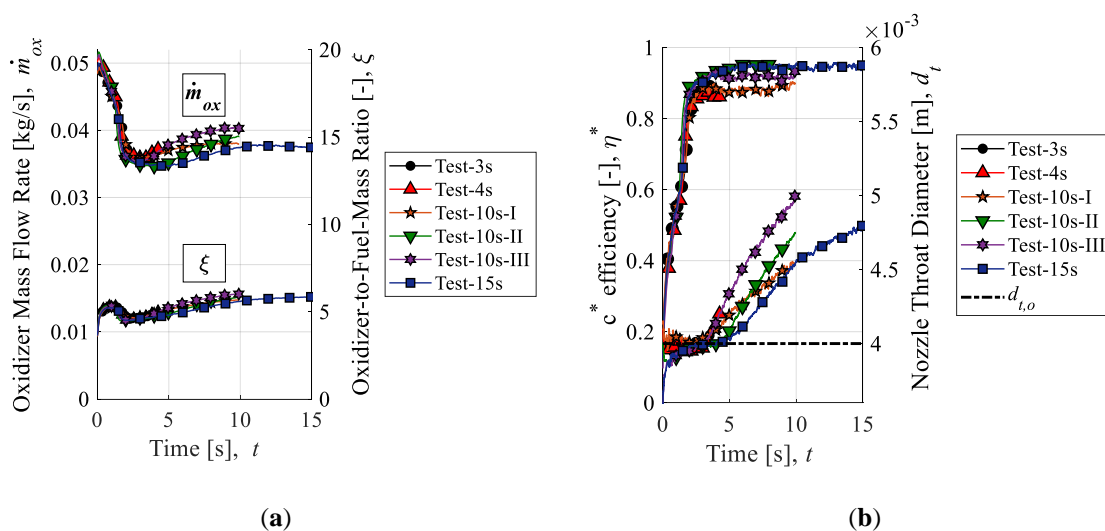

(**a**)　　　　　　　　　　　　　　(**b**)

Figure 10. The NTRT+ analysis (**a**) propellant flow rates; (**b**) throat erosion and efficiency histories.

Table 2. Summary of tier II (NTRT+) and tier III (TTRT) results.

Test Label	Local Name	λ	$\overline{\eta}^*$	$\overline{T}_w$ K	t_Π s	Φ	P_Π MPa	T_Π K
3s	(CBX-5)	0.97 ± 10%	0.87 ± 11%	1243 ± 9%	3	2.03 ± 4%	2.6 ± 2%	1778 ± 10%
4s	(CBX-4)	1.00 ± 10%	0.86 ± 10%	1464 ± 10%	3	2.02 ± 4%	2.6 ± 2%	2030 ± 12%
10s-I	(CBX-6)	0.97 ± 10%	0.88 ± 10%	1467 ± 10%	4	1.95 ± 4%	2.6 ± 2%	2076 ± 9%
10s-II	(CBX-8)	0.98 ± 9%	0.94 ± 9%	1455 ± 11%	5	1.96 ± 4%	2.7 ± 2%	1811 ± 7%
10s-III	(CBX-9)	0.90 ± 8%	0.91 ± 9%	1538 ± 10%	3	2.05 ± 4%	2.7 ± 2%	1963 ± 11%
15s	(CBX-7)	0.94 ± 8%	0.94 ± 10%	1527 ± 8%	5	1.95 ± 4%	2.7 ± 2%	1905 ± 7%

*time averages for η^* were taken after the first 3 s into the burn time to avoid startup transients.

3.3. Tier III Results: Results of the TTRT

Kamps et al. demonstrated in [27] that the wall temperature, pressure, and equivalence ratio at the nozzle throat can be used to predict whether or not thermochemical erosion may take place at the nozzle throat. This analysis will be shown in the following section, but first it is necessary to identify the temperature of nozzle throat wall using the TTRT. The results of the TTRT for time-averaged values of the nozzle throat wall temperature are listed in Table 2 as $\overline{T}w$ in K. Note that nozzle throat wall temperature histories could not be calculated for the entire burn time in most tests because the thermocouples nearest to the throat, predominately T_{5mm}, but in two occasions T_{check}, failed due to overheating. This typically happened around 5 s into the burn time. The results of the TTRT for nozzle throat wall temperature histories, T_w, in K are shown in red in Figure 11a. The two thermocouple measurement histories used as input data to the TTRT, at depths of 10 mm (T_{n2}) and 5 mm (T_{n1}) from the nozzle throat, are also shown in in Figure 11a in black and blue, respectively. The procedure for confirming the results of T_w is depicted in Figure 11b, where the thermocouple located at a depth of 8 mm from the nozzle throat (T_{check}) was used to verify the calculated value at that position within the nozzle. The solid black lines in Figure 11b show the calculated temperature profiles in the nozzle at 1 s intervals. The close agreement between calculated and measured values in Test-3s as shown in Figure 11b was also observed in all tests for the range of times where the thermocouples did not fail due to overheating.
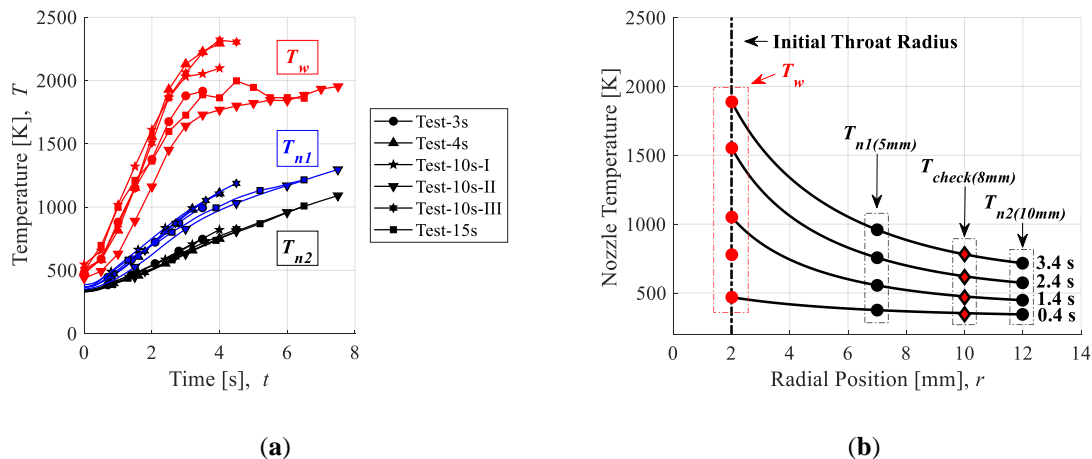

(a)　　　　　　　　　　　　　　　　　　　(b)

Figure 11. The TTRT analysis (**a**) nozzle temperature histories; (**b**) confirmation of temperature profile histories in Test-3s.

3.4. Erosion Onset Factor

The erosion onset factor, Π, was introduced by Kamps et al. in [27] as a way to model the nozzle temperature and gas pressure that allow for chemical kinetic-limited thermochemical erosion to take place for a given equivalence ratio, Φ—the ratio of the stoichiometric oxidizer-to-fuel mass ratio, ξ_{sto}

(ξ_{sto} = 9.4 for N$_2$O/HDPE), and the measured value of oxidizer-to-fuel mass ratio, ξ. Since the timing of the onset of erosion can be identified from Figure 10b, a brief analysis of Π will be conducted in this section. The equation for Π is (22):

$$\Pi = P^{n_\Pi} \exp(-E_\Pi / T_w) \tag{22}$$

where P is the local combustion gas pressure in Pa, n_Π is a dimensionless empirical constant, and E_Π is an empirical constant with units of K. Based on the results of [27], the following values of empirical constants will be used: n_Π = 1.03 and E_Π = 1408 K. Here, it is necessary to identify the pressure at the nozzle throat and the temperature of the nozzle throat wall position at the onset of nozzle throat erosion—listed as P_Π in Pa and T_Π in K in Table 2—so that values for the erosion onset factor may be calculated. The subscript, Π, is used to indicate the data taken at the time of the onset of erosion. Here, the value of P_Π was taken to be the pressure at the nozzle throat, P_t, which was approximated by the equation for the isentropic expansion of an ideal gas:

$$P_t = P_c \left(\frac{2}{\gamma + 1} \right)^{\frac{\gamma}{\gamma - 1}} \tag{23}$$

The times at the onset of erosion, t_Π, were chosen to be the time when the d_t histories in Figure 10b departed from the value of $d_{t,o}$ and had an erosion rate of more than 0.02 mm/s for longer than 1 s. The values for nozzle throat wall temperature at the onset of erosion were obtained from the T_w histories plotted in Figure 11a. The range of equivalence ratios, Φ, was not wide enough to carry out a correlation of Π, such as that in [27]. Thus, the data from [27] was used as a reference to evaluate the relative erosion characteristics observed in this study. Fortunately, there is a group of data and a trendline from [27] that lines up with the values of Φ observed in this study. This is shown in Figure 12. We can draw two useful conclusions from this comparison. The first conclusion is that even though nozzle erosion histories were not repeatable between tests in this study, the values of Π were. This suggests that the onset of erosion was essentially chemical-controlled. The second conclusion is that the use of N$_2$O in place of O$_2$ increased the threshold for Π. This is expected, since the presence of nitrogen in the combustion gas reduces the concentration of oxidizing species. Similar findings are reported by Bianchi and Nasuti regarding the difference in erosion rates when using N$_2$O as an oxidizer versus O$_2$ [21].
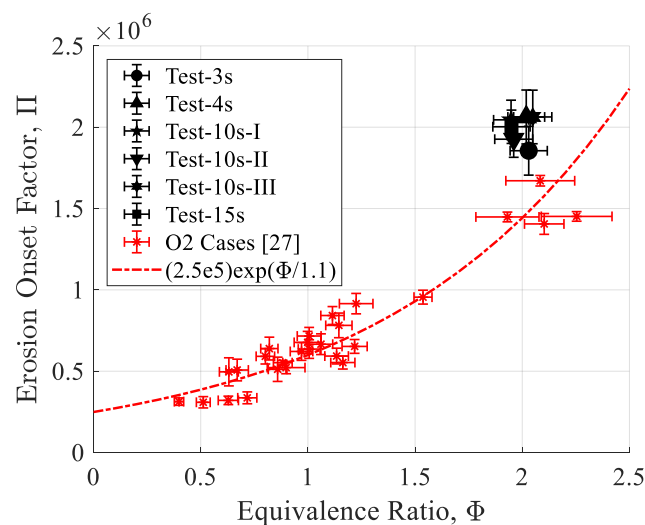

Figure 12. Erosion onset factor is larger when using N$_2$O as the oxidizer rather than O$_2$.

4. Conclusions

The propellant combination of nitrous oxide (N_2O) and high-density polyethylene (HDPE) shows promise for use in hybrid rocket apogee kick motors for the attributes of storability, non-toxicity, and stable burning with minimal combustion oscillations. However, there has been very little research published on the performance of hybrid rockets employing this propellant combination, and the research that has been made available to the public is limited in scope and inadequate for serious design considerations. This study introduces an improvement to well-tested non-intrusive data collection and analysis methods called ballistic reconstruction techniques in order to cost-effectively collect data on hybrid rockets using this propellant combination. The concept of this improvement is to introduce time-resolved fuel mass consumption into the governing equations of characteristic exhaust velocity and thrust, making it possible to simultaneously collect and evaluate time histories of the fuel regression rate, combustion efficiency, and nozzle throat erosion. The results were a highly cost-effective test series. With just six firing tests, the fuel regression rate could be correlated ($a = 2.52 \times 10^{-5}$; $n = 0.76$; such that the regression rate is in units of m/s), the combustion efficiency transients and trends became known (2 s transient; steady state values of 87% to 94%), and the erosion onset factor threshold was shown to be 50% larger than in the case where O_2 is used as the oxidizer. Moreover, now it is clearer how the chamber pressure, equivalence ratio, and nozzle heating transients at the beginning of a burn dictate when nozzle erosion is likely to begin.

Future implantation of the data reduction methodology introduced in this study will greatly expedite the development of hybrid rocket projects using N_2O/HDPE, including the apogee kick motor being developed by the authors. Essentially, all key aspects of combustion can be examined with a limited number of trials. This method may be especially helpful when studying the behavior of long-duration firing tests, for which neither time-averaged analysis methods nor high-resolution direct measurement techniques, such as X-ray radiography, are practical.

Author Contributions: This research was only possible through the collaboration and cooperation of all four of the authors, however, each author contributed in different ways to achieve the results reported in this paper. H.N. and L.K. held research responsibility for this work and the integration of these results within ongoing projects. This included the management of funds, ordering and receiving experimental equipment and managing experimental facilities. Y.S. and L.K. worked together extensively on the conceptualization and validation of the analysis methodology, and on the development of software for applying these methodologies. K.S. was the lead investigator, and was responsible for preparing and conducting the static firing tests together with L.K. and other graduate students from the University of Hokkaido. L.K. prepared the original draft of this manuscript, and all authors reviewed and edited this draft prior to submission.

Conflicts of Interest: The authors declare no conflict of interest.

Nomenclature

a,n	empirical constants of Equation (9)
A_e	nozzle exit area, m^2
A_t	nozzle throat area, m^2
C_{or}	dimensionless orifice flow coefficient
c_p	specific heat capacity of the nozzle, J/kg-K
c^*_{th}	theoretical characteristic exhaust velocity, m/s
d_e	nozzle exit diameter
D_{fu}	fuel outer diameter, m
d_{or}	orifice hole diameter, m
d_t	nozzle throat diameter, m

E_Π, n_Π	empirical constants of Equation (22)
F	thrust, N
G_{ox}	oxidizer port mass flux, kg/m^2-s
I_{sp}	specific impulse, s
k	thermal conductivity of the nozzle, W/m-K
L_{fu}	fuel length, m
M_{fu}	fuel mass, kg
m_{fu}	fuel mass consumption, kg
$\dot{m}$	propellant mass flow rate, kg/s
$\dot{m}_{ox}$	oxidizer mass flow rate, kg/s
P_a	atmospheric pressure, Pa
P_{dw}	orifice downstream pressure, Pa
P_e	nozzle exit pressure, Pa
P_t	nozzle throat pressure, Pa
P_{up}	orifice upstream pressure, Pa
P_v	vapor pressure (of N$_2$O), Pa
r_{fu}	fuel port radius, m
$\dot{r}_{fu}$	fuel (port) regression rate, m/s
t	time, s
t_b	burn time, s
T_w	nozzle wall temperature
U	experimental uncertainty
u_e	nozzle exit velocity, m/s
x, y	arbitrary input, output
Δr	radial mesh spacing, m
Δt	time step or data recording interval, s
α	thermal diffusivity of the nozzle, m^2/s
η^*	efficiency of c_{th}^*
γ	specific heat ratio of combustion gas
λ	thrust correction factor
Φ	equivalence ratio
Π	erosion onset factor
ρ_{ox}	oxidizer density, kg/m^3
ψ_d	nozzle throat diameter residual
ψ_F	thrust residual
ψ_T	thermocouple temperature residual
ξ	oxidizer-to-fuel-mass ratio
Additional Subscripts	
i	radial node index in Equations (14) & (15)
o, f	initial, final
w	nozzle wall position
$5mm, 8mm, 10mm$	thermocouples positioned 5 mm, 8 mm, and 10 mm from the nozzle throat
Π	specifies property at the onset of nozzle erosion
Additional Superscripts	
j	time index in Equations (14) & (15)
Acronyms	
CAMUI	Cascaded Multistage Impinging-jet
CEA	(NASA) Chemical Equilibrium with Applications
GFRP	Glass Fiber-Reinforced Plastic
GTO	Geostationary Transfer Orbit
HDPE	High-Density Polyethylene
ISAS	Institute of Space and Astronautical Science (Japan)
JAXA	Japan Aerospace Exploration Agency
NASA	National Aeronautics and Space Administration (USA)
NIST	National Institute of Standards and Technology (USA)
NTRT	Nozzle Throat Reconstruction Technique
PMMA	Polymethyl Methacrylate
TTRT	Throat Temperature Reconstruction Technique

References

1. The Wall Street Journal. Available online: https://www.wsj.com/articles/richard-bransons-space-tourism-company-rockets-out-of-atmosphere-for-first-time-11544720558 (accessed on 27 January 2019).

2.　Takahashi, A.; Shimada, T. Essentially Non-Explosive Propulsion Paving a Way for Fail-Safe Space Transportation. *Trans. JSASS Aerosp. Tech. Jpn.* **2018**, *16*, 1–8. [CrossRef]

3.　Altman, D.; Holzman, A. Overview and History of Hybrid Rocket Propulsion. In *Fundamentals of Hybrid Rocket Propulsion*, 1st ed.; Progress in Astronautics and Aeronautics; Chiaverini, M., Kuo, K., Eds.; AIAA: Washington, DC, USA, 2006; Volume 218, pp. 1–33. [CrossRef]

4.　Kuo, K.; Chiaverini, M. Challenges of Hybrid Rocket Propulsion in the 21st Century. In *Fundamentals of Hybrid Rocket Propulsion*, 1st ed.; Progress in Astronautics and Aeronautics; Chiaverini, M., Kuo, K., Eds.; AIAA: Washington, DC, USA, 2006; Volume 218, pp. 593–638. [CrossRef]

5.　Jens, E.T.; Cantwell, B.; Hubbard, G.S. Hybrid Rocket Propulsion Systems for Outer Planet Exploration Missions. *Acta Astronaut.* **2016**, *128*, 119–130. [CrossRef]

6.　Jens, E.T.; Karp, A.C.; Nakazono, B.; Vaughan, D.; Conte, A.; Contadin, S. Development Testing of Hybrid Rocket Motors Using Classical Fuels for Interplanetary CubeSats. In Proceedings of the 53rd AIAA/SAE/ASEE Joint Propulsion Conference, Atlanta, GA, USA, 10–12 July 2017. [CrossRef]

7.　Jens, E.T.; Karp, A.C.; Rabinovich, J.; Nakazono, B.; Conte, A.; Vaughan, D. Design of Interplanetary Hybrid CubeSat and SmallSat Propulsion Systems. In Proceedings of the 54th AIAA/SAE/ASEE Joint Propulsion Conference, Cincinnati, OH, USA, 9–11 July 2018. [CrossRef]

8.　Heister, S.; Wernimont, E. Hydrogen Peroxide, Hydroxyl Ammonium Nitrate, and Other Storable Oxidizers. In *Fundamentals of Hybrid Rocket Propulsion*, 1st ed.; Progress in Astronautics and Aeronautics; Chiaverini, M., Kuo, K., Eds.; AIAA: Washington, DC, USA, 2006; Volume 218, pp. 457–487. [CrossRef]

9.　NIST. Thermophysical Properties of Fluid Systems. Available online: https://webbook.nist.gov/chemistry/fluid (accessed on 1 August 2018).

10.　Story, G. Large-Scale Hybrid Motor Testing. In *Fundamentals of Hybrid Rocket Propulsion*, 1st ed.; Progress in Astronautics and Aeronautics; Chiaverini, M., Kuo, K., Eds.; AIAA: Washington, DC, USA, 2006; Volume 218, pp. 513–591. [CrossRef]

11.　Kobald, M.; Fischer, U.; Tomilin, K.; Petrarolo, A.; Schmierer, C. Hybrid Experimental Rocket Stuttgart: A Low-Cost Technology Demonstrator. *J. Spacecr. Rocket.* **2018**, *55*, 484–500. [CrossRef]

12.　Nakata, D.; Yasuda, K.; Horio, S.; Higashino, K. A Fundamental Study on the Hybrid Rocket Clustering for the Rocket Sled Propulsion System. In Proceedings of the 52nd AIAA/SAE/ASEE Joint Propulsion Conference, Salt Lake City, UT, USA, 25–27 July 2016. [CrossRef]

13.　Chen, Y.; Wu, B. Development of a Small Launch Vehicle with Hybrid Rocket Propulsion. In Proceedings of the 54th AIAA/SAE/ASEE Joint Propulsion Conference, Cincinnati, OH, USA, 9–11 July 2018. [CrossRef]

14.　Gamal, H.; Matusiewicz, A.; Magiera, R.; Hubert, D.; Karolewski, L.; Zielinski, K. Design, Analysis and Testing of a Hybrid Rocket Engine with a Multi-port Nozzle. In Proceedings of the 54th AIAA/SAE/ASEE Joint Propulsion Conference, Cincinnati, OH, USA, 9–11 July 2018. [CrossRef]

15.　Whitmore, S.; Peterson, Z.; Eilers, S. Closed-Loop Precision Throttling of a Hybrid Rocket Motor. *J. Propuls. Power* **2014**, *30*, 325–336. [CrossRef]

16.　Zilliac, G.; Waxman, B.; Evans, B.; Karabeyoglu, A.; Cantwell, B. Peregrine Hybrid Rocket Motor Development. In Proceedings of the 50th AIAA/SAE/ASEE Joint Propulsion Conference, Cleveland, OH, USA, 28–30 July 2014. [CrossRef]

17.　Nagata, H.; Wakita, M.; Totani, T.; Uematsu, T. Development and Flight Demonstration of 5 kN Thrust Class CAMUI Type Hybrid Rocket. *Trans. JSASS Aerosp. Tech.* **2014**, *12*, TA_1–TA_4. [CrossRef]

18.　Kamps, L.; Nagata, H. Tubular Equivalent Regression Rate in Hybrid Rockets with Complex Geometries. *Trans. JSASS* **2019**. [CrossRef]

19.　Mazzetti, A.; Merotto, L.; Pinarello, G. Paraffin-Based Hybrid Rocket Engines Applications: A Review and Market Perspective. *Acta Astronaut.* **2016**, *126*, 286–297. [CrossRef]

20.　Doran, E.; Dyer, J.; Lohner, K.; Dunn, Z.; Cantwell, B.; Zilliac, G. Nitrous Oxide Hybrid Rocket Motor Fuel Regression Rate Characterization. In Proceedings of the 43rd AIAA/SAE/ASEE Joint Propulsion Conference, Cincinnati, OH, USA, 8–11 July 2007. [CrossRef]

21.　Bianchi, D.; Nasuti, F. Numerical Analysis of Nozzle Material Thermochemical Erosion in Hybrid Rocket Engines. *J. Propuls. Power* **2013**, *29*, 547–558. [CrossRef]

22.　Wernimont, E.; Heister, D. Reconstruction Technique for Reducing Hybrid-Rocket Combustion Data. *J. Propuls. Power* **1999**, *15*, 128–136. [CrossRef]

23.　Nagata, H.; Nakayama, H.; Watanabe, M.; Wakita, M.; Totani, T. Accuracy and Applicable Range of a Range of a Reconstruction Technique for Hybrid Rockets. *Adv. Aircr. Spacecr. Sci.* **2014**, *1*, 273–289. [CrossRef]

24.　Carmicino, C.; Sorge, A. Influence of a Conical Axial Injector on Hybrid Rocket Performance. *J. Propuls. Power* **2006**, *22*, 984–995. [CrossRef]

25.　Nagata, H.; Saito, Y.; Ishiyama, T.; Inaba, Y.; Wakita, M.; Totani, T. Evaluations of Data Reduction Methods for Hybrid Rockets. In Proceedings of the 65th International Astronautical Congress, Toronto, ON, Canada, 29 September–3 October 2014.

26.　Kamps, L.T.; Saito, Y.; Kawabata, R.; Wakita, M.; Totani, T.; Nagata, H. Method for Determining Nozzle-Throat-Erosion-History in Hybrid Rockets. *J. Propuls. Power* **2017**, *33*, 1369–1377. [CrossRef]

27.　Kamps, L.; Hirai, S.; Sakurai, K.; Viscor, T.; Saito, Y.; Guan, R.; Isochi, H.; Adachi, N.; Itoh, M.; Nagata, H. Investigation of Graphite Nozzle Erosion in Hybrid Rockets Using O2/C2H4. In Proceedings of the 54th AIAA/SAE/ASEE Joint Propulsion Conference, Cincinnati, OH, USA, 9–11 July 2018. [CrossRef]

28.　Saito, Y.; Uematsu, T.; Isochi, H.; Wakita, M.; Totani, T.; Nagata, H. Estimation of Hybrid Rocket Nozzle Throat Erosion History. *Trans. JSASS* **2016**, *14*, 145–151. [CrossRef]

29.　Gordon, S.; McBride, B. *Computer Program for Calculation of Complex Chemical Equilibrium Compositions and Applications*; NASA RP-1311; NASA: Washington, DC, USA, 1994.

30.　Marxman, G.A.; Wooldridge, C.E.; Muzzy, R.J. Fundamentals of Hybrid Boundary-Layer Combustion. In *Heterogeneous Combustion*, 1st ed.; Progress in Astronautics and Aeronautics; Wolfhard, H.G., Glassman, I., Green, L., Eds.; AIAA: New York, NY, USA, 1964; Volume 15, pp. 485–522. [CrossRef]

31.　Sutton, G.; Biblarz, O. Solid Propellant Rocket Fundamentals. In *Rocket Propulsion Elements*, 8th ed.; Wiley: Hoboken, NJ, USA, 2010; pp. 435–489.

32.　G347 Graphite. Available online: https://www.tokaicarbon.co.jp/en/products/fine_carbon/pdf/Isotropic_graphite.pdf (accessed on 28 January 2019).

33.　Lutcov, A.I.; Volga, V.I.; Dymov, B.K. Thermal Conductivity, Electric Resistivity and Specific Heat of Dense Graphite. *Carbon* **1970**, *8*, 753–760. [CrossRef]

34.　Butland, A.T.D.; Maddison, R.J. The Specific Heat of Graphite: An Evaluation of Measurements. *J. Nucl. Mater.* **1973**, *49*, 49–56. [CrossRef]

35.　Rasband, W.S. *ImageJ*; U.S. National Institutes of Health: Bethesda, MD, USA, 1997–2018. Available online: https://imagej.nih.gov/ij/ (accessed on 3 August 2018).

36.　Kumar, C.P.; Kumar, A. Effect of Diaphragms on Regression Rate in Hybrid Rocket Motors. *J. Propuls. Power* **2013**, *29*, 559–572. [CrossRef]

37.　Kumar, R.; Ramakrishna, P.A. Enhancement of Hybrid Fuel Regression Rate Using a Bluff Body. *J. Propuls. Power* **2014**, *30*, 909–916. [CrossRef]

38.　DeLuca, L.T.; Galfetti, L.; Colombo, G.; Maggi, F.; Bandera, A.; Boiocchi, M.; Gariani, G.; Merotto, L.; Paravan, C.; Reina, A. Time-Resolved Burning of Solid Fuels for Hybrid Rocket Propulsion. *Prog. Propuls. Phys.* **2011**, *2*, 405–426. [CrossRef]

39.　Pavaran, C.; Reina, A.; Sossi, A.; Manzoni, M.; Massini, G.; Rambaldi, G.; Duranti, E.; Adami, A.; Seletti, E.; DeLuca, L.T. Time-Resolved Burning of Solid Fuels for Hybrid Rocket Propulsion. *Prog. Propuls. Phys.* **2011**, *2*, 405–426. [CrossRef]

40.　Evans, B.; Favorito, N.; Kuo, K. Oxidizer-Type and Aluminum-Particle Addition Effects on Solid-Fuel Burning Behavior. In Proceedings of the 42nd AIAA/SAE/ASEE Joint Propulsion Conference, Sacramento, CA, USA, 9–12 July 2006. [CrossRef]

41.　Chiaverini, M. Review of Solid-Fuel Regression Rate Behavior in Classical and Nonclassical Hybrid Rocket Motors. In *Fundamentals of Hybrid Rocket Propulsion*, 1st ed.; Progress in Astronautics and Aeronautics; Chiaverini, M., Kuo, K., Eds.; AIAA: Washington, DC, USA, 2006; Volume 218, pp. 37–116. [CrossRef]